Kapal: Jurnal Ilmu Pengetahuan dan Teknologi Kelautan
(Kapal: Journal of Marine Science and Technology)
journal homepage : http://ejournal.undip.ac.id/index.php/kapal
2301-9069 (e)
1829-8370 (p)

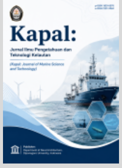

Experimental Study on the Hydrodynamic Resistance of a 265 GT Fishing Vessel with Wind-Assisted Propulsion

Anandita Fatihah1*), Rina2), Dian Purnama Sari2), Muhammad Ridwan Utina2), Wiwin Sulistyawati1)

1) Department of Naval Architecture, Pembangunan Nasional "Veteran" Jakarta University, Jakarta 12450, Indonesia
2) Research Center for Hydrodynamic Technology, National Research and Innovation Agency, Surabaya 60117, Indonesia
*) Corresponding Author: 2210313012@mahasiswa.upnvj.ac.id

Article Info

Keywords:
Fishing Vessel;
Wing Sail;
Wind-Assisted Ship Propulsion;
Towing Tank Experiment;
Resistance Characteristics;
Wind-Assisted Percentage (WA%)

Article history:
Received: 31/01/2026
Last revised: 30/03/2026
Accepted: 08/04/2026
Available online: 08/04/2026
Published: 09/04/2026

DOI:
https://doi.org/10.14710/kapal.v23i1.82101

Abstract

This study experimentally evaluates wind-assisted propulsion (WASP) to reduce the resistance of a 265 GT fishing vessel using model-scale towing tank test conducted at the PRTH-BRIN towing tank facility, with towing forces measured using calibrated resistance dynamometers following ITTC recommended procedures. Bare-hull resistance was measured at seven speeds over Froude numbers Fr ≈ 0.12 – 0.30, while tests with the wing sail installed were conducted at three speeds in the upper range (Fr ≈ 0.18 – 0.30) under steady beam wind conditions corresponding to a full-scale true wind speed of 20 knots. Towing-force measurements were converted into total resistance and total resistance coefficients. The wing sail effect was quantified using the wind-assisted percentage (WA%), defined as the relative reduction in resistance compared with the bare-hull condition at the same speed. A Type B uncertainty analysis following ITTC Recommendations was performed for the bare-hull measurements. The results show that, for the tested wind-assisted condition, the wing sail configuration produced lower resistance than the bare-hull at the same speed. The absolute resistance reduction increases with Froude number, reaching about 1.06 N at the highest speed, whereas WA% decreased from about 4.53% to 2.25% indicating a larger relative benefit at lower end of the tested speed range. The expanded relative uncertainty of bare-hull resistance is below 4% for all operating points. Overall, the experiments indicate a measurable wind-assisted contribution from the wing sail and provide a practical framework for assessing WASP performance at model scale using WA% as an indicator.

1. Introduction

The maritime industry is undergoing a significant transformation in response to global environmental challenges. With increasing pressure from international regulations, the maritime sector is required to reduce greenhouse gas emissions and the negative impacts associated by the use of fossil fuels [1]. Consequently, ship operators are seeking sustainable technologies to improve fuel efficiency and decrease fossil-fuel consumption. This transition is driven by international agreements, such as the IMO greenhouse-gas reduction strategy and MARPOL Annex VI regulations [2], [3]. The urgency of this transition is especially evident of the fishing sector, where reliance on fossil fuels is significant and alternative propulsion technologies have not been extensively implemented [4], [5], [6].

One of the technologies that has received growing attention is Wind-Assisted Ship Propulsion (WASP). By utilizing wind to provide additional thrust on ships, WASP reduces reliance on conventional propulsion and can lower fuel consumption and exhaust-gas emissions [7]. WASP offers an efficient and flexible way to harness wind energy, potentially reducing fuel cost, saving operational expenses, and contributing to emission reduction [8]. A wide variety of devices fall under the WASP umbrella. Including soft sail, rigid wing sail, flattener rotors and kites, each with different installation constraints and performance characteristic [9]. Recent design and performance studies further indicate that, when properly integrated, wing sail and rotor configurations can archive double-digit reductions in fuel consumption for suitable routes [10], [11]. Optimization research on rigid wing sail configurations has further validated their aerodynamic efficacy across various vessel types and operational conditions [12], [13].

Although wind-assisted propulsion is not a new concept, its application on medium to large fishing is still relatively unexplored. Fishing vessels operate in dynamic marine environments with unpredictable wind and wave conditions, so the integration of wind-assisted propulsion on these vessels requires more detailed study. Previous research on wind propulsion has mainly focused on merchant or large cargo ships [14], [15], while studies on small to medium-sized fishing vessels remain limited, particularly regarding the hydrodynamic and aerodynamic effect of wind propulsion under realistic environmental conditions [16]. In Indonesia, the fishing sector, which is heavily dependent on fossil fuels and challenged with rising operational expenses, urgently requires alternative propulsion sources [6]. The 265 GT vessel class is a category commonly used in Indonesian fishing waters, typically exhibiting modest service speeds with Froude numbers between Fr = 0.18 – 0.30, a range deemed appropriate for wind-assisted propulsion advantages [17]. However, no experimental research has methodically measured the decrease in hydrodynamic resistance due to a wing sail on this category of vessels. Understanding how wind propulsion interacts with the operational characteristics of medium-sized fishing vessels is therefore essential to advancing its adoption in this sector.

The present study contributes to this research gap by conducting model-scale resistance tests on a 265 GT fishing vessel, both with and without Wind-Assisted Propulsion. The experiments are performed in a towing tank to quantify effects of the wing sail system on resistance-based performance. Whereas many previous works have focused on larger cargo vessels, but research on small to medium-sized fishing vessels in varying environmental conditions are scarce [4], [16]. By comparing the resistance of the vessel with and without wing sail, this study aims to: (1) quantify the bare-hull resistance and total resistance coefficient of the 265 GT fishing vessel model across a Froude number range of Fr = 0.12 – 0.30; (2) evaluate the net resistance reduction due to the wing sail under steady beam wind conditions at Fr = 0.18 – 0.30; and (3) assess the wind-assisted percentage (WA%) as a normalized performance indicator for Wind-Assisted Propulsion at model scale, following the guidelines of the International Towing Tank Conference [18].

2. Method

2.1. Ship and Wind Propulsion Model

In this study, the ship model is scaled from a 265 GT fishing vessel full-scale for testing in the towing tank, both with and without Wind Assisted Propulsion. The ship model and wind-assisted propulsion system used in this study were adopted from a prior experimental research report developed at PRTH-BRIN [19], while the data processing and analysis were independently conducted in this present work. The ship model is designed to replicate the full-scale vessel while fitting the requirements for the towing tank experiment. The model vessel is scaled down using a 1: 9.685 scale ratio. This scaling follows similitude principles to ensure that model' s behavior in the towing tank reflects that of the full-scale vessel under real operational conditions [20]. To better understand the design of the model vessel, Figure 1 shows the ship model for the towing tank experiments.

Figure 1. The ship model

The lines plan of the full-scale 265 GT fishing vessel is presented in Figure 2, including the body plan, sheer plan, and half breadth plan. The hull design exemplifies a conventional displacement-type fishing vessel with a moderate beam-to-length ratio, characteristic of vessels operating in Indonesia fishing waters [17]. The lines plan verifies the design proportions specified in Table 1 and establishes the geometric foundation for the 1:9.685 scale model used in the towing tank experiments.

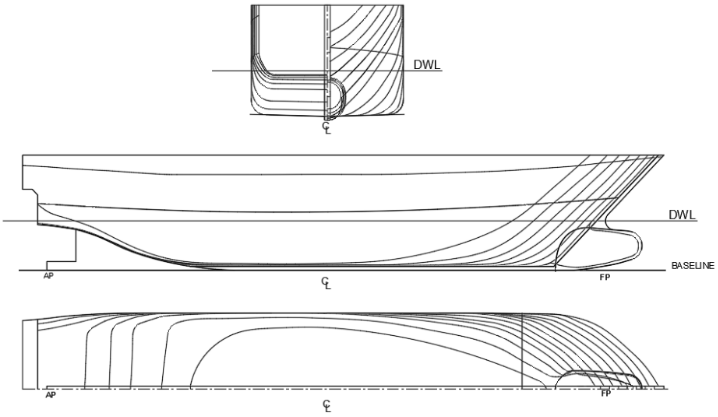

Figure 2. Lines plan of the full-scale 265 GT Fishing Vessel

Both the full-scale vessel and ship model share common design characteristics. The specifications for both the full-scale vessel and ship model are summarized in Table 1.

Table 1. Principal Particulars of Full-scale Vessel and Ship Model

Dimension	Notation	Full-scale Vessel	Ship Model
Length Overall	L_{OA} [m]	33.500	3.459
Length Between Perpendicular	L_{BP} [m]	29.054	3
Length Waterline	L_{WL} [m]	29.667	3.063
Breath	B [m]	7.950	0.821
Height	H [m]	6.026	0.622
Draft	T [m]	2.950	0.267
Displacement	[ton]	408.9	439.1
Gross Tonnage	GT [-]	265	-

The ship model is constructed using multiplex wood material. The hull design of the ship model closely follows the full-scale design to ensure that the flow characteristics and behavior of the ship model in water are accurately represented during testing. The wind propulsion device, specifically a wing sail, is employed to investigate the contribution wind-assisted propulsion in reducing resistance of the ship model. The wing sail design is based on aerodynamic principles similar to those of an aircraft wing, which generate lift and drag forces that can be controlled via the angle of attack [21]. Table 2 summarizes the specifications for the wing sail used in the experiments for both the full-scale vessel and the corresponding model.

Table 2. Principal Particulars of Full-scale Wing sail and Wing sail Model

Dimension	Notation	Full-scale Vessel	Ship Model
Wing sail Height [m]	H_{sail} [m]	7.3	0.754
Chord [m]	C [m]	2.85	0.294
Total Sail Area [m]	A_{sail} [m^2]	20.805	2.148
Number of Sail [m]	n_{sail} [-]	1	1

Figure 3 further illustrates the geometry of the full-scale wing sail and its scaled model, displaying the planform layout and cross-sectional profile of the NACA 0015 airfoil. The illustration validates the dimensional specifications presented in Table 2 and provides a visual representation of the sail geometry applied in the aerodynamic and hydrodynamic analysis performed in this study [22].

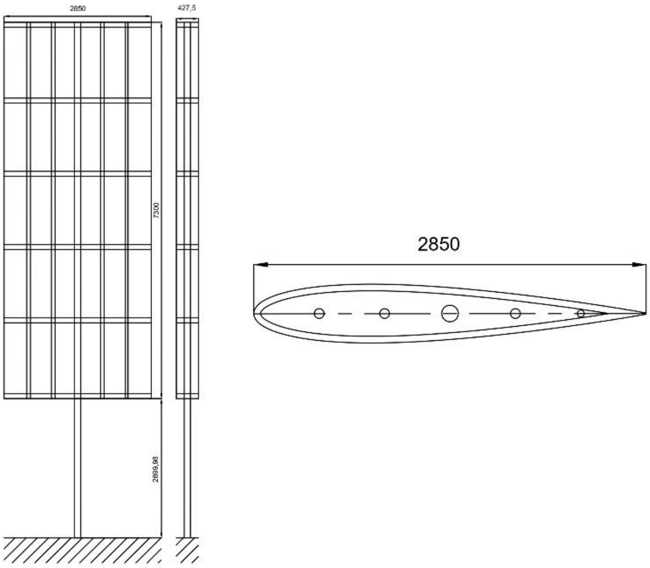

Figure 3. Geometry of the full-scale wing sail with NACA 0015 Airfoil Profile

The specifications for both the sail and model ship have been integrated to emphasize the proportional scaling between the model ship and the wing sail, ensuring that both are scaled consistently according to the 1: 9.685 ratio to accurately reflect the behavior of the full-scale vessel and wing sail. Figure 4 shows the wing sail model used in the experiment. It was designed using a NACA 0015 symmetric airfoil profile, which provides well-documented lift and drag characteristic for low-speed applications [23].

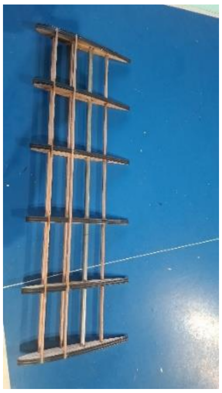

Figure 4. Wing sail model with NACA 0015 airfoil profile

The wing sail was installed at the centerline of the ship model, positioned at the midship section corresponding to the web frame 30 of the full-scale vessel. The wing sail structure′s base was attached directly to the main deck, with no modifications made to the hull geometry beneath the waterline. The centerline-midship placement was selected to minimize asymmetric lateral force impacts on the model during towing, and to ensure that the aerodynamic thrust contribution from the sail was predominantly aligned with the longitudinal axis of the vessel.

The ship model was prepared and ballasted to represent the hydrostatic condition of the full-scale vessel at the selected loading state. Prior to ballasting, the lightweight mass of the model was measured using a calibrated digital scale, yielding a value of 100.80 kg. Internal ballast weights were then installed to achieve the target draft and displacement corresponding to the geometric scale ratio of 9.685. The final ballasted mass of the model was 338.33 kg, which represents a scaled displacement of 439.13 kg.

2.2. Experimental Setup

The resistance tests were conducted using a scale model of a 265 GT fishing vessel equipped with a wind-assisted wing sail. All experiments were carried out in the towing tank facility of the Hydrodynamics Laboratory in Badan Riset Inovasi Nasional (PRTH), Surabaya [19], [24]. The experimental procedure follows standard ITTC guidelines for resistance tests [18]. The towing tank specifications are detailed in Table 3.

Table 3. Towing Tank Specification

Specification	Value	Unit
Length	234.5	Meter
Breadth	11	Meter
Depth	5.5	Meter
Model Ship Length	3-9	Meter

Carriage Speed (min to max)	0.2 – 9	m/s
Maximum Flow Rate	Up to 12	m/s
Maximum Carriage Acceleration	1	m/s^2
Working Pressure	0.2 - 2	bar

The water temperature during the tests was maintained at 27.6°C, corresponding to a kinematic viscosity of 8.317 × 10^{-7} m^2/s [25]. All instrumentation used in the resistance test was calibrated prior to testing and traceable to international standards through the National Accreditation Committee of Indonesia (KAN, accreditation number LK-023-IDN). The primary instruments and their specifications are summarized in Table 4.

Table 4. Principal Instrumentation Used in the Resistance Tests

Instrument	Type/Model	Range	Expanded Uncertainty (k=2)
Resistance Dynamometer	R-56	0-50 kg	±0.028 kg
External Load Cell (Wind-Assisted)	Lorenz Messtechnik S-type Tension Compression	0-10 kg	-
Towing Speed Sensor	SCANDAS (NI-based)	0-9 m/s	0.107 m/s (2×SEE)
Water Thermometer	PTM-806 Type K	-50-1300 °C, res. 0.1 °C	0.18 °C
Electronic Hanging Scale	CCS-600	0-600 kg, res. 0.2 kg	0.11 kg
Stopwatch	HS-70W	-	0.038 s

Note: Expanded uncertainty for the external load cell is not reported as uncertainty analysis was performed exclusively for the bare-hull configuration, as described in **Section 2.5**.

Two force-measurement instruments were employed in this study, each corresponding to a different test configuration. A R-56 resistance dynamometer with a capacity of a 50 kg was used for the bare-hull resistance test. The dynamometer was calibrated using standard dead-weight procedures traceable to international standards. In the wind-assisted configuration, an external load cell replaced the R-56 dynamometer. This substitution was necessary because the experimental setup required additional space on the deck and internal volume of the model to accommodate the wing sail structure and its mounting configuration, which was incompatible with the installation footprint of the R-56. The external load cell used for the wind-assisted configuration was a Lorenz Messtechnik S-type tension-compression load cell with a capacity of 10 kg. Both instruments were linked to a National Instruments-based SCADAS data acquisition system functioning at a sampling rate of 50 Hz. The recorded force signals from both configurations were processed using a low-pass filter with a cut-off frequency of 10 Hz to suppress high-frequency disturbances, before time-averaging over the steady-state interval to obtain the representative towing force for each test conditions.

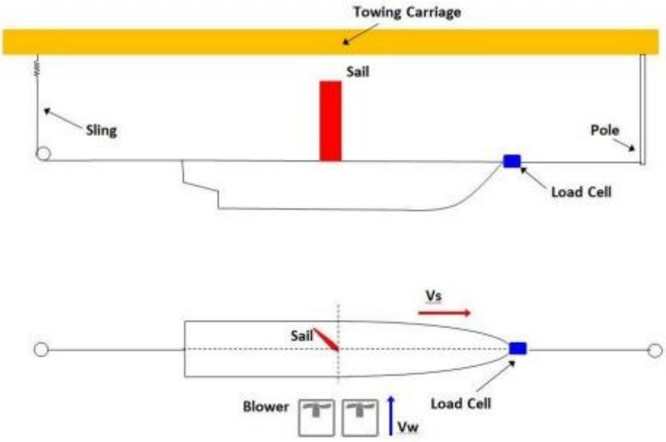

Figure 5. Experimental Setup Diagram

For each test condition, the carriage was smoothly accelerated until the desired steady velocity was achieved. Once the motion of the model became stable, towing force data were recorded and the steady-state portion of the signal was retained for analysis. Each test configuration was performed once, as the primary objective of this study was to characterize the resistance behavior under different wind-propulsion arrangements rather than to assess statistical repeatability. The complete experimental layout and the two model configurations (bare-hull and wing sail-assisted) are shown in Figure 5.

In addition to the primary towing instrumentation, several auxiliary components were incorporated to enable the wind-assisted test configuration. A blower unit was installed on the towing carriage to supply a controlled and uniform airflow toward the wing sail during the wind-assisted tests. The airflow was aligned with the model centerline, and the blower output was maintained at a constant setting for all relevant test conditions. A light tension sling was connected between the carriage side frame and the model bow to limit excessive yaw motion under high sail loading; the sling remained slack during straight towing and engaged only when lateral displacement occurred. The general arrangement of the blower, tension sling and external load cell follows layouts used in previous wind-assisted towing tank experiments, but was modified to fit the present towing tank facility and model dimensions [26].

Figure 6. Resistance test at Towing tank

Figure 6 present the resistance test in progress at the PRTH-BRIN Towing Tank. Figure 7 illustrates the overall perspective of the resistance test performed at the PRTH-BRIN Towing Tank facility. The figure depicts the comprehensive configuration of the experiment, featuring the towing carriage situated above the tank, the ship model buoyant in the water, and the instrumentation apparatus affixed to the carriage. This documentation verifies that the experimental circumstances were physically implemented as described in the preceding sections, with the model accurately positioned and the measuring apparatus completely constructed before each test run.

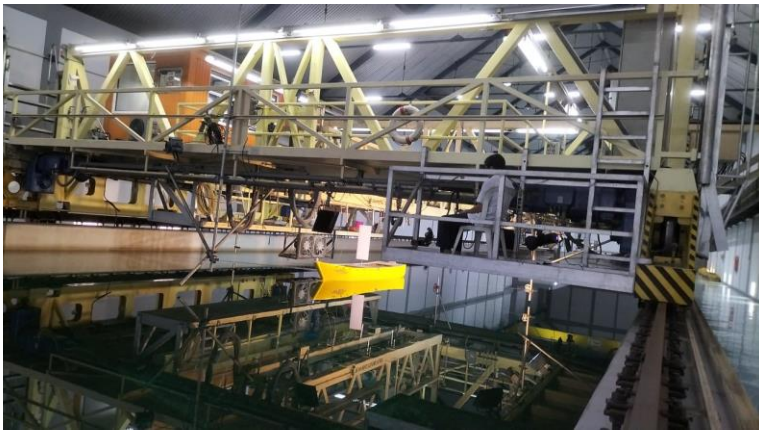

Figure 7. General view of the resistance test arrangement at the PRTH-BRIN Towing Tank facility.

The blower arrangement employed to produce airflow during the wind-assisted test is illustrated in Figure 8. The fan array was affixed directly to the towing carriage frame and directed at the sail position on the model. This configuration guaranteed that the produced airflow consistently aligned with the model's centerline during each test run, resulting in stable and reproducible wind conditions at the sail site. The blower was used at a consistent pre-calibrated setting for all wind-assisted test conditions, as previously outlined.

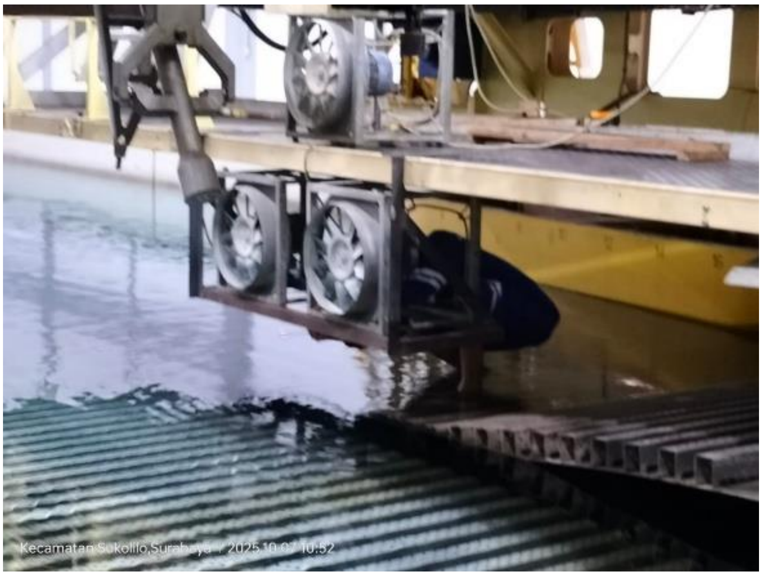

Figure 8. Blower unit mounted on the towing carriage

(Source: Technical Report PRTH-BRIN 2025)

Before the wind-assisted test runs, the wind speed at the sail location was confirmed using a portable anemometer positioned at the base of the wing sail mast, as illustrated in Figure 9. The anemometer was used solely during the pre-test calibration phase to verify that the blower output achieved the necessary wind speed of 3.305 m/s at the sail position. This approach guaranteed that the wind condition affecting the sail was uniform and reproducible across all tested configurations.

Figure 9. Portable anemometer mounted at the base of the wing sail mast

Figure 10 presents a detailed perspective of the ship model in the wind-assisted test configuration. The wing sail is distinctly positioned at the model′ s centerline in the midship location, in accordance with specifications outlined in Section 2.1. This picture also illustrates the external load cell connection at the model bow, validating the instrumentation configuration employed to assess the net towing resistance in wind-assisted conditions. Figure 10 illustrates the comprehensive wind-assisted test configuration from which the resistance reduction and WA% outcomes detailed in Section 3 were obtained.

Figure 10. Ship model with wing sail installed during the wind-assisted resistance test

2.3. Test Procedure

The model was towed at a series of prescribed velocities corresponding to Froude numbers between 0.12 and 0.30. Each run started with a smooth acceleration until the target speed was reached, followed by a constant-speed measurement segment. Only the steady-state portion of the recorded signals was used for analysis, in accordance with the ITTC recommended procedure for resistance test [18]. All test conditions were conducted once; repeatability assessment was not included in the scope of this study.

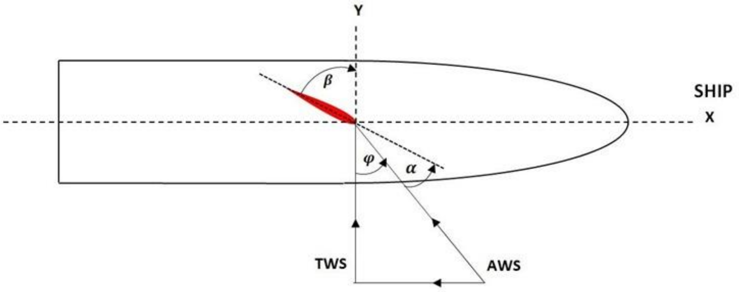

Figure 11. Definition of wind and sail angles used in this study

Figure 11 defines the wind-related angles and velocities used in this study. The ship-fixed coordinate system is defined with the X-Axis pointing forward and the Y-Axis pointing to port. The incoming flow generated by the blower is treated as the True Wind Speed (TWS), while the ship speed is the towing velocity. The Apparent Wind Speed (AWS) and its direction are obtained from the vector combination of TWS and ship speed. The true wind angle (TWA) is defined as the angle between the ship heading (X-Axis) and the true wind direction; in the present setup the wind was applied from the side (beam wind), corresponding to TWA = 90°. The wing sail setting angle (β) denotes the orientation of the sail relative to the ship transverse axis (Y-Axis) and follows the values specified in the test matrix; for the present test, the sail position was at β = 30°, meaning that the sail was rotated 30° form the transverse direction. The angle of attack (α) is defined as the angle between the apparent wind direction (AWS) and the wing sail chord line. i.e., the apparent wind angle is the ship-fixed frame referenced to the sail setting angle β (with the sign convention consistent with Figure 11). The angle of attack values reported in Table 5 correspond to the entries listed under the symbol α.

Two configurations were evaluated, as summarized in Table 5: a bare-hull configuration and a wing sail-assisted configuration. For the bare-hull tests, the wing sail model and blower were removed while maintaining the same ballast condition, tow-point position, and instrumentation arrangement. In the wind-assisted test, the wing sail was installed at the predetermined location as described in Section 2.2 and the blower was operated to generate a nominally steady wind. The wind speed at the sail position was monitored and maintained at a target value of 3.305 m/s for all wind-assisted runs. This value was selected based on wind climatology data for the southern Java Sea and surrounding waters, where surface winds exhibit significant seasonal variability associated with the monsoon system [27]. In the Benoa, Bali fishing ground specifically, wind speeds can reach up to 20 knots under certain seasonal conditions, representing a practically relevant upper-bound condition for wind-assisted propulsion assessment on this vessel class. The model-scale wind speed of 3.305 m/s was therefore selected to replicate this upper-bound full-scale condition of 20 knots via Froude scaling. No adjustment to underwater geometry, ballast, or tow-point arrangement were made between configurations, so that differences in measured towing force reflected the effect of the wing sail under the specified wind-assisted condition [28].

Table 5. Test matrix for resistance measurements

Configuration	Fr	V_{sm} (m/s)	β (deg)	α (deg)	V_{wm} (m/s)	TWA (deg)
Bare-hull	0.121	0.661	-	-	-	-
	0.151	0.827	-	-	-	-
	0.181	0.992	-	-	-	-
	0.211	1.157	-	-	-	-
	0.241	1.322	-	-	-	-
	0.271	1.488	-	-	-	-
	0.302	1.653	-	-	-	-
Wing sail Assisted	0.181	0.992	30	13.32	3.306	90
	0.241	1.322	30	8.23	3.306	90
	0.302	1.653	30	3.46	3.306	90

Table 5 summarizes the complete test matrix, including the tested Froude numbers, corresponding towing speeds, sail setting angle, and wind condition. All quantities in Table 5 refer to model-scale conditions consistent with ITTC procedures for dynamic similarity. No full-scale conversions were applied within this section, as the objective is to provide a controlled comparison of total resistance between the bare-hull and wing-sail configurations.

2.4. Data Acquisition and Analysis

Hydrodynamic resistance measurements were obtained from towing experiments based on the measured towing force and carriage speed. All force signals were recorded using a calibrated load-cell system, and only the steady-state portion of each towing run was used in the analysis. The recorded signals were filtered to remove high-frequency disturbances and subsequently time-averaged to obtain representative force values for each test condition.

The total resistance R_T of the model was taken directly from the measured towing force. To enable comparison across speeds, the total resistance coefficient was computed as [18]:

$$C_T = \frac{R_T}{\frac{1}{2}\rho S_m V^2} \tag{1}$$

where ρ is the water density, V the towing speed, and S_m the wetted surface area of the model geometry (hydrostatic calculation) at the design draft. The corresponding Froude number was calculated as:

$$F_r = \frac{V}{\sqrt{gL}} \tag{2}$$

where L is the characteristic length of the model defined in **Section 2.1**.

All comparisons were performed at identical towing speeds to enable direct comparison between the bare-hull and wing sail-assisted conditions. To evaluate the influence of wing sail installation on the measurement resistance, the resistance reduction was defined as the difference between the bare-hull resistance and the resistance measured with the wing sail installed:

$$\Delta \mathrm{R} = R_{T,bare} - R_{T,wing} \tag{3}$$

where $R_{T,bare}$ is the measured resistance of the ship model under bare-hull configuration without wing sail, and $R_{T,wing}$ denotes the resistance measured with the wing sail configuration. To further quantify the relative contribution of the wing sail to the overall longitudinal force balance, a wind-assistance percentage (WA%) was defined following the thrust-based formulation proposed in the literature [14]. In the present towing-tank experiments, the longitudinal thrust condition generated by the wing sail, $F_{X,sail}$ was not measured directly but inferred from the reduction in measured towing resistance between the bare-hull and wing sail-assisted configurations, i.e. $F_{X,sail} = \Delta\mathrm{R}$. The remaining thrust demand, T, corresponds to the measured towing resistance under the wing sail-assisted condition. The wind-assisted percentage is the define as:

$$WA\% = \left(\frac{F_{X,sail}}{F_{X,sail} + T}\right) \times 100\% \tag{4}$$

This parameter represents the relative reduction in towing resistance attributable to the wing sail at model scale. The processed resistance data and derived performance metrics obtained through the above procedures form the basis for uncertainty assessment and performance evaluation presented in the following sections.

2.5. Uncertainty Analysis

This section′ s uncertainty evaluation pertains solely to the bare-hull resistance measurements acquired with the R-56 dynamometer. An equivalent uncertainty evaluation for the wind-assisted arrangement was not conducted in this study. The uncertainty assessment adheres to the ITTC Recommended Procedures for resistance uncertainty analysis [29]. The uncertainty estimate, consistent with the methodology applied in the Indonesian Hydrodynamic Laboratory [30], incorporates Type B contributions derived from instrument specifications and ancillary information. In addition, a Type A component was included to represent within-run variability of steady-state towing-resistance signal. Since each experiment program was conducted only once per operating point, repeatability between repeated runs was not considered.

Accordingly, the uncertainty components reported in this work comprise systematic (Type B) contributions, complemented by a statistical (Type A) term obtained from the recorded steady-state signal. Four primary sources of Type B uncertainty were taken into account: load-cell calibration, towing speed measurement, water temperature effects on water properties (density and kinematic viscosity), and model displacement estimation. In addition, the Type A within-run variability of towing resistance, u_R (R_T) was calculated from the standard deviation of the measured towing-resistance signal within the steady-state interval of each run, and expressed in relative form. Table 6 summarizes the uncertainty components and symbols used in this study; the calculated values are reported in **Section 3.3.**

Table 6. Uncertainty components for towing resistance

Source of Uncertainty	Symbol
Load cell	u_{LC}
Towing speed	u_V
Water temperature	u_{Temp}
Model displacement	u_{Disp}
Single run force variability	u_R

The combined relative standard uncertainty of towing resistance R_T was calculated using the root-sum-square (RSS) method assuming independent components:

$$u_{c,rel}(R_T) = \sqrt{u_{LC}^2 + u_V^2 + u_{Temp}^2 + u_{Disp}^2 + u_R^2} \tag{5}$$

where all u_i are expressed as relative values in percent. The expanded relative uncertainty was then computed as:

$$U_{rel}(RT) = k\, u_{c,rel}(RT) \tag{6}$$

with a coverage factor $k = 2$, corresponding to a confidence level of approximately 95%. The absolute expanded uncertainty of the resistance was obtained as:

$$U(RT) = U_{rel}(RT)RT \tag{7}$$

Since the nondimensional resistance coefficients C_T are directly proportional to R_T, the same relative uncertainty $U_{rel}(RT)$ applies to C_T when evaluated using the same instrumentation and data acquisition procedures. The within-run Type A uncertainty term was defined as:

$$u_R = \frac{\sigma R_T}{\bar{R}_T} \times 100\% \tag{8}$$

where σR_T is the standard deviation of the towing resistance signal within the steady-state interval, and $\bar{R}_T$ is the mean towing resistance over the same interval.

This evaluation accounts for the contributions of load-cell accuracy, towing-speed measurement, water-property variability, and model displacement tolerances, as well as the within-run variability of the measured signal. The resulting uncertainty bounds support the reliability of the resistance measurements and the derived performance indicators within the tested condition. An uncertainty bound for WA% is not reported in the present study due to absence of repeated runs and the limited uncertainty characterization for the wind-assisted condition.

3. Results and Discussion

3.1. Bare Hull Resistance

Figure 12 present the variation of the bare-hull total resistance as a function of Froude number over the range Fr = 0.12 – 0.30. The experiments were conducted over a Froude number range of Fr = 0.12 – 0.30. Within this range, measured resistance increases smoothly and monotonically with Froude numbers, indicating stable towing condition and consistent measurements.

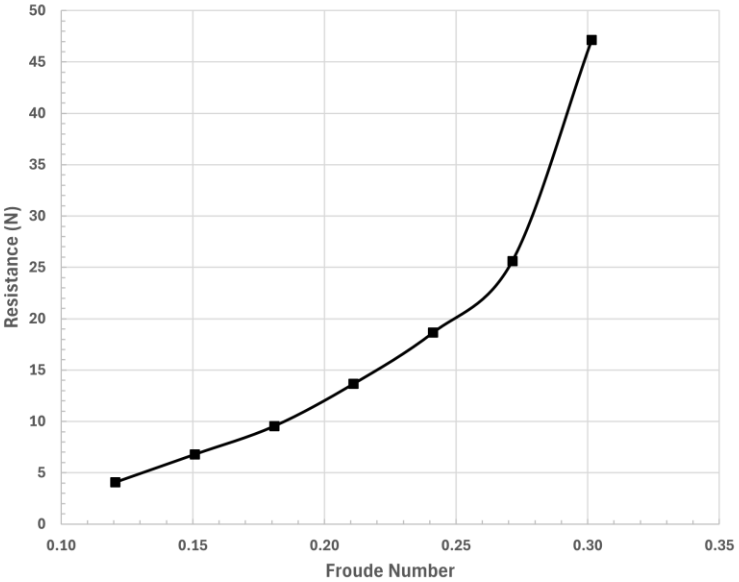

Figure 12. Bare-hull total resistance as a function of Froude number

At lower Froude numbers, the increase in resistance is relatively gradual. As the Froude number approaches the upper part of the tested range, a noticeable change in the slope of the resistance curve is observed, indicating a non-linear resistance trend that is commonly reported for displacement hulls operating from low to moderate Froude numbers. Similar non-linear resistance growth has been reported for comparable fishing vessel hull forms by [31], who confirmed through both experimental and CFD analysis that resistance increases more steeply at higher Froude numbers due to growing wave-making contributions. The present bare-hull results align with this established behavior, confirming that the tested hull form demonstrates typical characteristics of displacement vessels within the examined Froude number range. This trend is typically linked to the increasing influence of wave-related effects as speed increases, although no component separation is attempted in the present study.

To remove the dominant speed dependance and facilitate comparison across operating points, the results are also expressed in nondimensional form as the total resistance coefficient, shown in Figure 13. The coefficient remains within a relatively narrow band at lower Froude numbers and then increases markedly toward Fr ≈ 0.30, which supports the observed non-linear trend in the dimensional resistance.

No abnormal fluctuation or discontinuities are identified in either the total resistance or total resistance coefficient curves, and the overall behavior is consistent with established hydrodynamics characteristics of conventional displacement hulls. The bare-hull resistance results therefore provide a reliable bare-hull for the subsequent assessment of the wing sail-assisted configuration discussed in the following section.

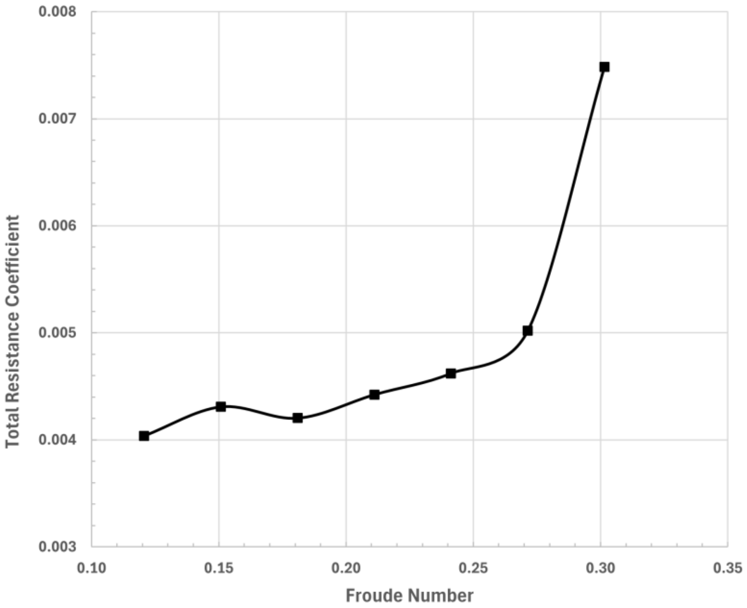

Figure 13. Bare-hull total resistance coefficient (CT) as a function of Froude number

3.2. Resistance with Wing sail Installed

Figure 14 compares the measured towing resistance between the bare-hull configuration and the wing sail configuration under the wind-assisted condition at the selected operating points. For all tested wind-assisted speeds, the measured resistance with the wing sail installed is lower than the corresponding bare-hull resistance at the same Froude number. The resistance reduction increases with towing speed in absolute terms. At Fr ≈ 0.18, the resistance decreases from 9.54 N (bare-hull) to 9.10 N (wing sail), corresponding to a reduction of about 0.43 N. At Fr ≈ 0.24, the resistance decreases from 18.3 N to 17.8 N, giving a reduction of roughly 0.5 N. At the highest tested speed, Fr ≈ 0.30, the resistance decreases from 47.0 N to 45.9 N, corresponding to a reduction of about 1.1 N.

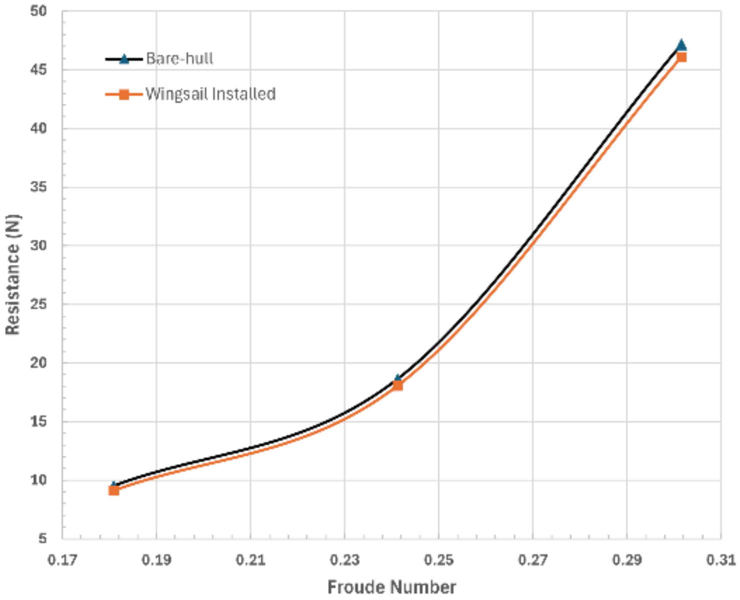

Figure 14. Comparison of bare-hull and wing sail installed total resistance as a function of Froude number

Although the absolute resistance reduction increases with Froude number, the relative impact of the wing sail decreases at elevated speeds, a phenomenon elaborated upon concerning the wind-assisted percentage WA% in **Section 3.4.** It should be noted that the measured resistance reflects the net longitudinal force balance on the model, which includes the combined hydrodynamic effect and the aerodynamics interaction induced by the wind and wing sail. Therefore, the observed reductions are interpreted as net reductions in towing demand under the specified wind-assisted condition rather than a direct measurement of aerodynamics thrust. These results form the basis for evaluating wind-assisted performance using the wind-assisted percentage (WA%) in the following section.

3.3. Uncertainty of the Resistance Measurements

The uncertainties associated with the towing resistance measurement were evaluated according to the procedure described in **Section 2.5.** The Type B relative components calculated from instrument calibration/specification following the ITTC procedure summarized in Table 7. For each towing speed, the within-run variability term u_R was computed from steady-state scatter of towing resistance signal and combined with the Type B components using RSS method to obtain $u_{c,rel}(RT)$. The expanded relative uncertainty $U_{rel}(RT)$ was then calculated using a coverage factor $k = 2$ (approximately 95% confidence), and the corresponding absolute expanded uncertainty was obtained as $U(RT)$. The uncertainty results for each towing speed are reported in Table 8.

Table 7. Type B uncertainty components for towing resistance

Source of Uncertainty	**Symbol**	**Relative uncertainty (%)**
Load cell	u_{LC}	0.775
Towing speed	u_V	0.100
Water temperature	u_{Temp}	0.007
Model displacement	u_{Disp}	0.342

Table 8. Combined and expanded uncertainty of towing resistance measurements for each towing speed

V (m/s)	$\boldsymbol{u_R}$ **(%)**	$\boldsymbol{u_{c,rel}(RT)}$ **(%)**	$\boldsymbol{U_{rel}(RT)}$ **(%)**	$\boldsymbol{U(RT)}$ **(kgf)**
0.661	0.10	1.75	3.51	0.0155
0.827	0.09	1.09	2.17	0.0156
0.992	0.07	0.78	1.57	0.0157
1.157	0.06	0.55	1.11	0.0158
1.322	0.05	0.41	0.83	0.0161
1.488	0.05	0.31	0.61	0.0166
1.653	0.02	0.19	0.37	0.0184

The expanded relative uncertainties $u_{c,rel}(RT)$ range from approximately 3.5% and 0.4% over the investigated speed range. The maximum value of 3.51% occurs at the lowest towing speed, while the relative uncertainty decreases monotonically with increasing speed. In absolute terms, the expanded uncertainty $U(RT)$ remains nearly constant over the investigated speed range, varying slightly from approximately 0.0155 kgf to 0.0184 kgf as the resistance increases.

These uncertainty levels are consistent with typical model-scale towing tank measurements and indicate that the observed differences between the bare-hull and wing sail configurations can be interpreted with reference to the reported uncertainty bounds. Accordingly, the resistance trends and the derived performance indicators are discussed in the subsequent section while acknowledging the uncertainty limits reported herein.

3.4. Wind Assisted Percentage (WA%)

To provide a normalized indicator of the wing sail contribution, the wind assisted percentage (WA%) was evaluated based on the resistance-reduction definition described in Section 2.4. Figure 15 presents WA% as a function of Froude number for the tested wind-assisted operating points ($Fr \approx 0.18 - 0.30$). WA% is positive at all tested points, indicating a consistent net benefit in terms of resistance reduction.

The WA% values decrease from 4.53% at lower Froude numbers to 3.16% at intermediate point and 2.25% at the highest tested Froude number. This trend indicates that, while the absolute resistance reduction increases with speed, the relative contribution of the wing sail becomes smaller toward higher Froude numbers within the tested range. No resistance-component decomposition is performed in the present study; therefore, the trend is discussed in terms of the measured total resistance behavior.

The decreasing trend of WA% with increasing Froude number can be understood by considering two concurrent effects. First, for the displacement hull functioning within the moderate Froude number range examined here, total resistance increases non-linearly with velocity due to the increasing influence of wave-making resistance at elevated speeds, as confirmed for similar fishing vessel hull configurations by [31]. The aerodynamic thrust produced by the wing sail varies with the tested speeds, as the apparent wind angle changes with increasing ship speed while the true wind speed remains constant. Table 5 illustrates that the angle of attack decreases from 13.32° at Fr 0.18 to 3.46° at Fr 0.30. At reduced angles of attack, a symmetric NACA 0015 airfoil functions at a distance from its optimal lift-to-drag ratio, resulting in diminished net longitudinal thrust for equivalent true wind input [14], [23]. The interplay of increasing hydrodynamic resistance as denominator and diminishing aerodynamic thrust contribution as numerator elucidates the observed decline in WA% at elevated Froude numbers.

In the context of the existing literature, rigid sail system on larger commercial vessels have been reported to provide fuel savings ranging from 5% to 60% depending upon vessel size, route, wind availability, and number of sails installed [5]. The WA% range of 2.25% to 4.53% identified in the present study is at the lower end of this spectrum, aligning with the experimental conditions used: a single sail of relatively small area tested under single fixed wind condition at model scale. With more advantageous apparent wind angles or with optimized sail setting, the WA% contribution would be expected to increase, consistent with the higher lift-to-drag ratio achievable by the NACA 0015 profile at more favorable angles of attack[24]. Guzelbulut et al. [14] demonstrated through a model-based methodology utilizing a NACA 0015 rigid sail that the percentage decrease in energy consumption at a velocity of 5 m/s under beam wind conditions is significantly greater than at 7 m/s, thereby confirming that the speed-dependent reduction in WA% is an intrinsic attribute of wind-assisted propulsion systems rather than a constraint particular to this study.

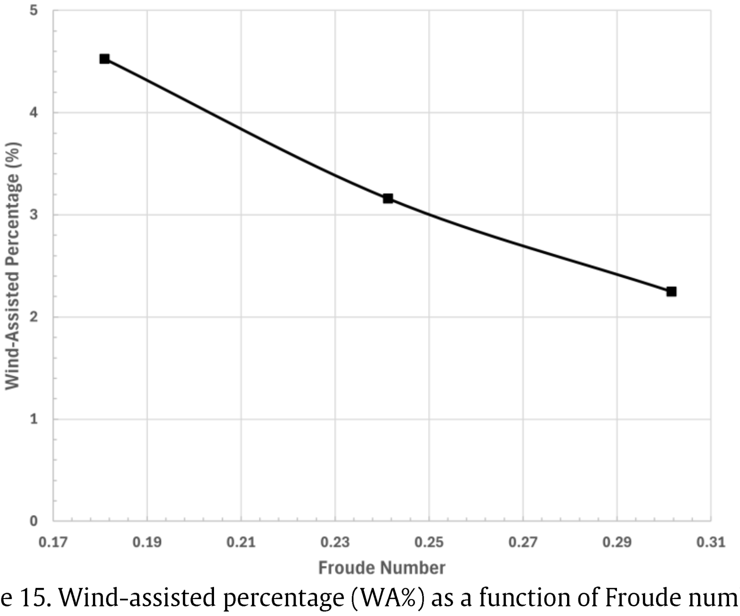

Figure 15. Wind-assisted percentage (WA%) as a function of Froude number

3.5. Integrated Discussion (Hydro-Aero Interaction)

The experimental result demonstrate that the installation of a wing sail leads to a consistent reduction in the measured towing resistance across the tested wind-assisted operating points. This reduction is reflected in both the absolute resistance difference (ΔR) and the wind-assisted percentage (WA%), indicating a measurable contribution of wind-assisted propulsion at model scale. The observed trends highlight the different interpretations provided by absolute and relative performance metrics. While the absolute resistance reduction increases with towing speed, the corresponding WA% decreases with increasing Froude number. This behavior is consistent with the non-linear increase of total resistance toward higher Froude numbers, which reduces the relative magnitude of the wind-assisted effect. From a practical perspective, these results suggest that the relative benefit of wing-assisted propulsion is more pronounced at lower operating speed, where total resistance increases more gradually within the tested range. At higher speeds, although the wing sail continues to provide a beneficial net contribution, its relative impact diminishes as total resistance increases more steeply toward the upper Froude number range.

From a hydrodynamic standpoint, the resistance reduction observed in the wind-assisted configuration reflects the cumulative impact of two opposing mechanisms. The aerodynamic force produced by the wing sail operates in the longitudinal direction and partially counteracts the pulling force necessary to sustain the specified speed, as evidenced by the observed decreased in towing resistance. The wing sail structure concurrently generates additional aerodynamic drag on the above-water segment of the model, exerting force in the opposite direction. The reported reduction in net resistance at all three tested speeds suggests that the longitudinal thrust component surpassed the parasitic drag of the sail apparatus under the current experimental conditions. This balance is influenced by the angle of attack, which in this experiment range from 13.32° at Fr 0.18 to 3.46° at Fr 0.30, since the apparent wind angle shifted with increasing ship speed at fixed true wind speed. The diminishing angle of attack at elevated speeds indicates that the sail was functioning increasingly away from its optimal aerodynamic state, aligning with the observed decline in WA% and results from numerical analyses on NACA 0015 rigid sails under comparable beam wind conditions [14], [21].

The trends observed in the present study are consistent with findings reported in the literature on wind-assisted propulsion systems. Full-scale performance datasets, such as those reported by [5], indicate that the relative contribution of wind-assisted propulsion decreases with increasing vessel speed under resistance-dominated operating conditions. Likewise, Hosseinzadeh et al. [32] illustrated through self-propulsion experiments on wind-assisted vessels that the relative thrust contribution from wind assistance diminishes as total resistance becomes increasingly sensitive to speed under elevated operating conditions, owing to the growing influence of hull-propeller-rudder interaction effects. The model-based analysis by [14] confirmed that, at a constant true wind speed and beam wind direction, an increasing in ship speed reduces the apparent wind angle and, consequently, the effective angle of attack of the rigid sail, resulting in reduce thrust output and a diminished relative contribution to propulsion. The concordance between the current experimental trend and these independent computational and experimental results corroborates the physical reality of the WA% behavior reported in this study.

It is emphasized that the present finding is based on resistance-based performance metric derived from towing-tank measurement. As no direct aerodynamic force measurements were performed, the result represents the net effect of combined hydrodynamics and aerodynamics interactions rather than isolated aerodynamic performance. Nevertheless, the adopted methodology provides a practical framework for assessing wind-assisted propulsion concepts at model scale. The observed trends remain clearly distinguishable within the experimental uncertainty bounds described in Section 3.3 (see Section 2.5. for details of the uncertainty evaluation procedure).

4. Conclusion

This study experimentally investigated the hydrodynamic resistance of a 265 GT fishing vessel equipped with a NACA 0015 wing sail wind-assisted propulsion system through model-scale towing tank test. The bare-hull resistance increases non-linearly with Froude number over the tested range of Fr = 0.12 to 0.30, exhibiting behavior consistent with displacement hull characteristics reported in comparable fishing vessel studies. The installation of the wing sail under steady beam wind conditions corresponding to a full-scale true wind speed of 20 knots produced a measurable net reduction in towing resistance at all three evaluated wind-assisted speeds, with absolute reductions ranging from approximately 0.43 N at Fr = 0.18 to 1.06 N at Fr = 0.30. The wind-assisted percentage WA% decreased from 4.53% at Fr = 0.18 to 2.25% at Fr = 0.30, indicating that the relative benefit of wind assistance is more pronounced at lower operating speeds where the rate of increase in total resistance is more gradual. This speed-dependent pattern is physically consistent with concurrent reduction in apparent wind angle and aerodynamic angle of attack as ship speed increases at fixed true wind speed, and is in agreement with trends reported in independent experimental WASP studies.

The expanded relative uncertainty of the bare-hull resistance measurements remained below 4% at all tested operating points, confirming the reliability of the experimental results. Overall, these findings demonstrate that even a single wing sail design can provide a measurable and quantifiable resistance reduction for a fishing vessel hull form representative of the 265 GT class, supporting the technical feasibility of wind-assisted propulsion as part of a broader fuel-efficiency strategy for the Indonesian fishing fleet, and providing an experimental reference for future work in full-scale performance forecasting, sail configuration optimization, and coupled hydro-aero numerical analysis.

Acknowledgements

The authors also gratefully acknowledge PRTH-BRIN team for providing access to the experimental data and for their technical assistance during the research activities. Experimental activities in the towing tank were made possible with the help of the research team and workshop staff at Research Center for Hydrodynamic Technology, who provided the facilities and operational support used in this study.

References

[1] R. Irvana, K. Abdullah, A. S. Uyun, and O. Anne, 'Transformation Conventional Fishing Vessels 30 GT to Hybrid (Diesel-PV) System to Reduce Fuel Oil Consumption and Exhaust Emissions', *BIO Web Conf.*, vol. 104, p. 00033, May 2024, doi: https://doi.org/10.1051/bioconf/202410400033.

[2] K. Yeremenko, 'International Maritime Organization and Decarbonization of Maritime Industry: Mandate and Instruments', *Lex Portus*, vol. 8, no. 3, pp. 30–57, Jul. 2022, doi: https://doi.org/10.26886/2524-101X.8.3.2022.2.

[3] International Maritime Organization, 'Fourth Greenhouse Gas Study', 2020.

[4] A. I. Sultoni, M. M. Ali, and Z. P. Aji, ‵Hybrid Propulsion System (PV / Gasoline) For Small Fishing Vessels′, *Kapal: Jurnal Ilmu Pengetahuan dan Teknologi Kelautan*, vol. 17, no. 1, pp. 1–6, Feb. 2020, doi: https://doi.org/10.14710/kapal.v17i1.25613.

[5] M. Kolodziejski and M. Sosnowski, ‵Review of Wind-Assisted Propulsion Systems in Maritime Transport′, *Energies (Basel)*., vol. 18, no. 4, p. 897, Feb. 2025, doi: https://doi.org/10.3390/en18040897.

[6] A. Buwono, M. Muslim, R. Irvana, S. Manullang, R. Dariansyah, and A. C. Partahi Oloan, ‵Initial Engineering Studies of Battery Capacity Prediction Power of ‶Electric Ship of FTK UNSADA″ Container Concept from Jakarta to Ibu Kota Nusantara′, *Kapal: Jurnal Ilmu Pengetahuan dan Teknologi Kelautan*, vol. 21, no. 2, pp. 112–126, Aug. 2024, doi: https://doi.org/10.14710/kapal.v21i2.64620.

[7] V. Vigna and M. Figari, ‵Wind-Assisted Ship Propulsion Feasibility Study′, 2022. doi: https://doi.org/10.3233/PMST220003.

[8] A. D. Maimon, ‵Wind propulsion of ships to decarbonize maritime transport′, *Analele Universităţii ‵Dunărea de Jos′ din Galaţi Fascicula XI Construcţii navale/ Annals of ‵Dunărea de Jos′ of Galati Fascicle XI Shipbuilding*, vol. 46, pp. 55–60, Dec. 2023, doi: https://doi.org/10.35219/AnnUgalShipBuilding/2023.46.07.

[9] L. Khan, J. J. R. Macklin, B. C. D. Peck, O. Morton, and J.-B. R. G. Souppez, ‵A Review of Wind-Assisted Ship Propulsion for Sustainable Commercial Shipping: Latest Developments and Future Stakes′, *Wind Propulsion 2021*, Sep. 2021.

[10] F. Thies and J. W. Ringsberg, ‵Wind-assisted, electric, and pure wind propulsion – the path towards zero-emission RoRo ships′, *Ships and Offshore Structures*, vol. 18, no. 8, pp. 1229–1236, Aug. 2023, doi: https://doi.org/10.1080/17445302.2022.2111923.

[11] T. Chou, V. Kosmas, M. Acciaro, and K. Renken, ‵A Comeback of Wind Power in Shipping: An Economic and Operational Review on the Wind-Assisted Ship Propulsion Technology′, *Sustainability (Switzerland)*, vol. 13, no. 4, pp. 1–16, Feb. 2021, doi: https://doi.org/10.3390/su13041880.

[12] T. Plessas and A. Papanikolaou, ‵Multi-Objective Optimization of Ship Design for the Effect of Wind Propulsion′, *Journal of Marine Science and Engineering*, vol. 13, no. 1, p. 167, Jan. 2025, doi: https://doi.org/10.3390/jmse13010167.

[13] A. Yasuda, T. Taniguchi, and T. Katayama, ‵Numerical Investigation of Aerodynamic Interactions between Rigid Sails Attached to Ship′, *Journal of Marine Science and Engineering*, vol. 12, no. 8, p. 1425, Aug. 2024, doi: https://doi.org/10.3390/jmse12081425.

[14] C. Guzelbulut, T. Sugimoto, Y. Fujita, and K. Suzuki, ‵Investigation of the efficiency of wind-assisted systems using model-based design approach′, *Journal of Marine Science and Technology*, vol. 29, no. 2, pp. 387–403, Jun. 2024, doi: https://doi.org/10.1007/s00773-024-00993-6.

[15] N. J. van der Kolk, J. A. Keuning, and R. H. M. Huijsmans, ‵Part 1: Experimental Validation of a RANS-CFD Methodology for the Hydrodynamics of Wind-Assisted Ships Operating at Leeway Angles′, *Ocean Engineering*, vol. 178, pp. 375–387, Apr. 2019, doi: https://doi.org/10.1016/j.oceaneng.2018.12.041.

[16] T. Sauder and S. A. Alterskjær, ‵Hydrodynamic Testing of Wind-Assisted Cargo Ships Using a Cyber–Physical Method′, *Ocean Engineering*, vol. 243, p. 110206, Jan. 2022, doi: https://doi.org/10.1016/j.oceaneng.2021.110206.

[17] R. B. Luhulima, S. Sutiyo, and I. K. A. P. Utama, ‵CFD Analysis into the Resistance of Trimaran with Longitudinal Sidehull Adjustments′, *Kapal: Jurnal Ilmu Pengetahuan dan Teknologi Kelautan*, vol. 18, no. 3, pp. 119–127, Oct. 2021, doi: https://doi.org/10.14710/kapal.v18i3.41010.

[18] ITTC, ‵ITTC Recommended Procedure 7.5-02-02-01: Resistance Test (Rev. 05)′, 2021.

[19] P. Dian, M. R. Utina, Rina, S. Endah, and S. Nanang, ‵Model Experiment on Fishing Vessel Operation in Benoa, Bali, Using Wind-Assisted Propulsion System′, Surabaya, 2025.

[20] K. Wrzask, ‵On the Vessel Energy Requirement Prediction From the Acceleration Stage Towing Experiments on Models′, Apr. 2023, [Online]. Available: http://arxiv.org/abs/2308.04200

[21] H. Wu, S. Yang, C. Liu, and G. Xiang, ‵Design & Performance Analysis of Variable Cross-section Wing Sail Based on Discrete Deformation Structure′, *IFAC-PapersOnLine*, vol. 59, no. 22, pp. 764–769, Aug. 2025, doi: https://doi.org/10.1016/j.ifacol.2025.11.727.

[22] A. Amiadji, A. Baidowi, I. S. Arief, and F. P. Ricinzky, ‵CFD Based Analysis of Resistance and Pitch Motion of Novel Flat Plate Panel Hull Vessel′, *Kapal: Jurnal Ilmu Pengetahuan dan Teknologi Kelautan*, vol. 19, no. 1, pp. 9–22, Feb. 2022, doi: https://doi.org/10.14710/kapal.v19i1.43370.

[23] i. şahin and A. Acir, ‵Numerical and Experimental Investigations of Lift and Drag Performances of NACA 0015 Wind Turbine Airfoil′, *International Journal of Materials, Mechanics and Manufacturing*, vol. 3, no. 1, pp. 22–25, 2015, doi: https://doi.org/10.7763/IJMMM.2015.V3.159.

[24] A. Winarno, G. A. N. S. Sakti, and E. Sugianto, ‵The Effect of Tip Clearance Kaplan Ducted Propeller in Offshore Supply Vessel (OSV) on Hydrodynamics′, *Kapal: Jurnal Ilmu Pengetahuan dan Teknologi Kelautan*, vol. 21, no. 3, pp. 156–170, Oct. 2024, doi: https://doi.org/10.14710/kapal.v21i3.64772.

[25] ITTC, ‵ITTC Recommended Procedure 7.5-02-01-03: General Density and Viscosity of Water (Rev. 01)′, 2006.

[26] N. T. H. Trang, T. Mitsuyuki, Y. Hirakawa, K. Sadakata, and Y. Nakamura, ‵Experimental and Numerical Study on the Seakeeping Performance of a Wind-Powered Generation Ship Considering Boom Configurations′, *J. Mar. Sci. Eng*., vol. 13, no. 3, p. 412, Feb. 2025, doi: https://doi.org/10.3390/jmse13030412.

[27] I. Sofiati, E. Yulihastin, Suaydhi, and M. F. Putranto, 'Meridional Variations of Sea Surface Temperature and Wind Over Southern Sea of Java and its Surroundings', *Journal of Physics and Its Applications*, vol. 3, no. 1, pp. 129–135, 2020, doi: https://ejournal2.undip.ac.id/index.php/jpa/article/view/9374.

[28] R. Eggers and A. S. Kisjes, 'Seakeeping and Manoeuvring for Wind Assisted Ships', *Wind Propulsion 2019*, Oct. 2019.

[29] ITTC, 'ITTC Recommended Procedure 7.5-02-02-02: General Guideline for Uncertainty Analysis in Resistance Tests (Rev.03)', 2021.

[30] I. K. A. P. Utama, D. Purnamasari, I. K. Suastika, Nurhadi, and G. A. Thomas, 'Toward Improvement of Resistance Testing Reliability', *Journal of Engineering and Technological Sciences*, vol. 53, no. 2, 2021, doi: https://doi.org/10.5614/j.eng.technol.sci.2021.53.2.1.

[31] S. Oyuela, H. R. D. Ojeda, F. P. Arribas, A. D. Otero, and R. Sosa, 'Investigating Fishing Vessel Hydrodynamics by Using EFD and CFD Tools, with Focus on Total Ship Resistance and Its Components', *Journal of Marine Science and Engineering*, vol. 12, no. 4, p. 622, Apr. 2024, doi: https://doi.org/10.3390/jmse12040622.

[32] S. Hosseinzadeh, D. Hudson, S. R. Turnock, M. Prince, and J. Banks, 'Influence of Hull–Propeller–Rudder Interaction on the Self-Propulsion of Wind-Assisted Ships', *Physics of Fluids*, vol. 37, no. 8, p. 087216, Aug. 2025, doi: https://doi.org/10.1063/5.0281083.